Coastal Engineering 68 (2012) 44–55

Contents lists available at SciVerse ScienceDirect

Coastal Engineering

journal homepage: www.elsevier.com/locate/coastaleng

Radiation stress and low-frequency energy balance within the surf zone: A numerical approach

Andrea Ruju *, Javier L. Lara, Inigo J. Losada

Environmental Hydraulics Institute "IH Cantabria", Universidad de Cantabria, C/Isabel Torres 15 Parque Cientifico y Tecnologico de Cantabria, 39011 Santander, Spain

A R T I C L E   I N F O

Article history:
Received 17 October 2011
Received in revised form 8 May 2012
Accepted 10 May 2012
Available online 2 June 2012

Keywords:
Radiation stress
Energy balance
Long wave dissipation
Surf zone
RANS

A B S T R A C T

This paper evaluates the energy transfer between short and long waves resulting from nonlinear interactions of the radiation stress with the low-frequency motion in the nearshore. Shoaling and breaking of irregular waves over different slopes are investigated by means of numerical simulations with the Reynolds Averaged Navier–Stokes model IH-2VOF. The low-frequency energy flux is enhanced up to the outer surf zone where dissipation starts. Seaward of the inner surf zone, the rate of work done by the radiation stress roughly balances the low-frequency energy flux gradients, indicating that nonlinear interactions with sea–swell waves are responsible for both the enhancement and the damping of low-frequency energy. In the inner surf zone, interactions between short- and long-wave fields are weak and the low-frequency energy loss appears to be largely due to self–self nonlinear interactions.

1. Introduction

Wave motions at sea and swell frequencies represent the main forcing of the nearshore circulation. As swells approach the shore, a large amount of energy is nonlinearly transferred from the peak of the incident wave spectrum to both higher- and lower-frequency waves. On natural beaches, the breaking process causes strong dissipation of energy contained in the sea–swell and higher-frequency bands. On the other hand, due to their low wave steepness, subharmonic waves usually experience both small energy dissipation inside the surf zone and strong reflection at the shoreline. As a result, low-frequency oscillations often dominate the wave motion in the inner surf and in the swash zone (Guza and Thorton, 1982; Huntley, 1976).

Munk (1949) and Tucker (1950) reported for the first time the presence of free surface oscillations at short-wave group periods and coined the term "surf beat" for such low-frequency motions (also the term "infragravity waves" is now widely used). Longuet-Higgins and Stewart (1962) successfully explained the mechanics of infragravity waves identifying the forcing in the radiation stress gradient related to short-wave groups outside the surf zone. It is well accepted that inside the surf zone, where the radiation stress decreases and groupiness is strongly damped out, long waves bound to wave groups are not destroyed but they are likely to be released as free waves. Another different (and complementary) generation mechanism of surf beat was proposed by Symonds et al. (1982). According to that theory, the forcing is represented by the radiation stress gradient related to short-wave breaking in that part of the nearshore which intermittently lies in the surf zone as a result of the oscillations of the breakpoint.

The Longuet-Higgins and Stewart (1962) and Symonds et al. (1982) theories have revealed the importance of radiation stress in surf beat generation. Energy transfer between short and long waves occurs as a result of the work done by the radiation stress (Phillips, 1977; Schäffer, 1993), yielding a growth rate of the forced long waves potentially exceeding the rate predicted by the Green's law (conservative shoaling). Moreover, inside the surf zone, infragravity energy losses have been observed in field, laboratory as well as numerical experiments (Baldock et al., 2000; Battjes et al., 2004; Madsen et al., 1997; Sheremet et al., 2002; Torres-Freyermuth et al., 2010). Although bottom friction acts over the entire domain to dissipate wave energy (Henderson and Bowen, 2002), it seems that breaking of long waves (van Dongeren et al., 2007) and negative work done by the radiation stress (Henderson et al., 2006; Thomson et al., 2006) are the main agents for most of low-frequency energy dissipation observed inside the surf zone.

Despite its theoretical and practical importance, only few publications dealing with infragravity waves have reported a quantitative evaluation of radiation stresses and their relation with infragravity motions. In many laboratory experiments, see for example Baldock and Huntley (2002) and Janssen et al. (2003), the forcing of infragravity motion is usually inferred from the short-wave envelope as a consequence of the difficulty in obtaining the sufficiently detailed velocity field measurements by means of customary instruments. In particular, Battjes et al. (2004) provided a quantitative energy balance analysis in the shoaling zone but they could not extend it to the surf zone due to the assumptions involved in the radiation stress estimation.

* Corresponding author.
E-mail address: rujua@unican.es (A. Ruju).

0378-3839/$ – see front matter © 2012 Elsevier B.V. All rights reserved.
doi:10.1016/j.coastaleng.2012.05.003

The aim of this work is to perform a quantitative description of the cross-shore evolution of the radiation stress in order to evaluate the energy transfer between short and long waves in the nearshore. We take advantage of the refined information provided by the numerical model IH-2VOF (Lara et al., 2011) to carry out a detailed energy balance both outside and inside the surf zone. The results of a set of numerical simulations for random wave cases over a sloping bottom are presented and discussed. In particular, this work addresses two important topics in nearshore hydrodynamics such as low-frequency energy damping inside the surf zone and long-wave reflection at the shoreline. These processes, in spite of the increasing attention received in the last decade, are still not completely understood. In this paper the role played by the different low-frequency energy damping agents is analyzed in order to identify which damping mechanism prevails within the surf zone.

The paper is organized as follows. Section 2 describes the numerical model. The analysis techniques are provided in Section 3. Section 4 illustrates the results for the irregular wave cases. Conclusions are outlined in Section 5.

2. Numerical model

2.1. Model description

The numerical model IH-2VOF (Lara et al., 2011), an updated version of COBRAS-UC (Losada et al., 2008), solves the two dimensional 2DV Reynolds Averaged Navier–Stokes (RANS) equations with a turbulence closure model. Applying the Reynolds decomposition for turbulent flows, the instantaneous velocity and pressure fields are decomposed into mean and turbulent components. The influence of turbulence fluctuations on the mean flow is represented by the Reynolds stress tensor which is related to the strain rate of mean flow through a nonlinear algebraic Reynolds stress model (Lin and Liu, 1998; Rodi, 1980). The problem is closed using a $k-\varepsilon$ model (Jones and Launder, 1972) with higher-order correlations of turbulence fluctuations in k and replaced by closure conditions (Shih et al., 1996). The free surface movement is tracked by the Volume of Fluid (VOF) method.

The use of a RANS model is motivated, amongst other different numerical approaches, because nonlinearity and wave breaking are directly solved with no pre-imposed assumptions. Several wave generation procedures are implemented into the IH-2VOF model. An exhaustive description of the strength and weakness of each method can be found in previous publications (Lara et al., 2011; Losada et al., 2008; Torres-Freyermuth et al., 2010). In this work the moving boundary method is used in order replicate the action of a piston type wave generator.

2.2. Model set-up

A new set of numerical experiments is carried out over a geometry reproducing a physical wave flume. The working water depth h_0 is fixed at 0.4 m during the experiments. The fixed, smoothed bathymetry is made up of a horizontal bottom part that extends up to the toe of the beach located at 10.64 m from the wave maker and a constant slope part that reaches the end of the flume. Two plane beaches with a slope h_x of 1:20 and 1:30 are introduced in order to resemble relatively steep profiles (the incoming wave conditions considered in Section 4.1 lead to relative bottom slopes $S = h_x L_0 / h_0$, L_0 being the wave length in the generation region, ranging between 0.23 and 0.34). The origin of the co-ordinate system is fixed at the intersection of the still water level with the bottom, with the horizontal axis positive shoreward. The bottom profiles for the two slopes are shown in Fig. 1.

The numerical mesh is 0.6 m high extending up to 0.2 m (see the reference system introduced). In the horizontal direction it extends from 1 m behind the zero position of the wave maker up to the point where the vertical coordinate of the bottom profile reaches the value of 0.1 m. The grid system provides a uniform spatial resolution Δz of 0.5 cm in the vertical direction while the horizontal resolution Δx varies from 1.2 cm in the generation region to 0.8 cm in the swash zone. The time step, automatically adjusted during the simulation to fulfill the stability conditions, lies between 10^{-4} and 10^{-2} s in the simulated cases. The time required to simulate 10 s is of the order of an hour in a standard PC.

2.3. Model validations

The IH-2VOF model has been mainly used in investigations addressing wave-structure interactions (Guanche et al., 2009; Lara et al., 2008; Losada et al., 2008). In addition, the model has been successfully applied to simulate surf zone hydrodynamics on prototype (Torres-Freyermuth et al., 2007) as well as laboratory (Torres-Freyermuth et al., 2010) gently sloping beaches. More recently, Lara et al. (2011) investigated long-wave forcing by a transient wave group focused at the breakpoint of the short waves. The detailed validations provided by the mentioned studies have attested the ability of the IH-2VOF model to satisfactorily reproduce the surf zone processes subject to different wave conditions and bottom profiles for both laboratory and field cases. As a consequence, in this work, the simulated wave cases are not contrasted with new laboratory experiments for validation and we refer to the validation provided by Lara et al. (2011). In particular, we present numerical experiments carried out over comparable spatial domains with the same mesh resolution. Furthermore, Lara et al. (2011), hereinafter referred to as L11, considered wave conditions characterized by an Iribarren number $I_r = h_x / \sqrt{H_0/L_0}$ (H_0 and L_0 being the wave height and wave length in the generation region) ranging between 0.21 and 0.44. Referring back to that study, in the present work we propose an analogous set of I_r varying between 0.21 and 0.43, see Section 4.1. Table 1 compares the relevant geometrical parameters involved in L11 and in the present work, denoted by PW. MR refers to "Mesh Resolution" in Table 1.

Summing up, the present numerical experiments are designed in strict analogy with the experiments carried out and validated by L11 in order to ensure the necessary reliability of the results presented and discussed in Section 4.

3. Analysis techniques

3.1. Decomposition techniques

In the classical approach, the depth-integrated nearshore circulation equations are averaged over a short-wave period in order to study the slowly varying component of motion (Mei, 1989; Phillips, 1977; Svendsen, 2005). Here we address the problem in a slightly different way and we separate the free surface and horizontal velocity fields into a short-wave and a long-wave (or current) part by means of a low-pass filter. The use a low-pass filter appears particularly suitable when dealing with irregular waves.

Considering the case of normally incident waves, the separation of the free surface η and the horizontal velocity u into low- and high-frequency components yields:

$$\eta = \|\eta\|_{(lf)} + \eta_w = \eta_c + \eta_w \tag{1}$$

$$u = \frac{1}{h+\eta_c} \left\| \int_{-h}^{\eta} u dz \right\|_{(lf)} + u_w = U + u_w \tag{2}$$

where h is the still water depth, η_c and η_w denote the low-frequency and high-frequency free surface displacement, u_w is the horizontal short-wave velocity and U is the horizontal slowly-varying current. The long-wave component $\|\cdot\|_{lf}$ is obtained by means of a Fourier-filtered low-pass time series with a cut-off frequency of $f_p/2$, in

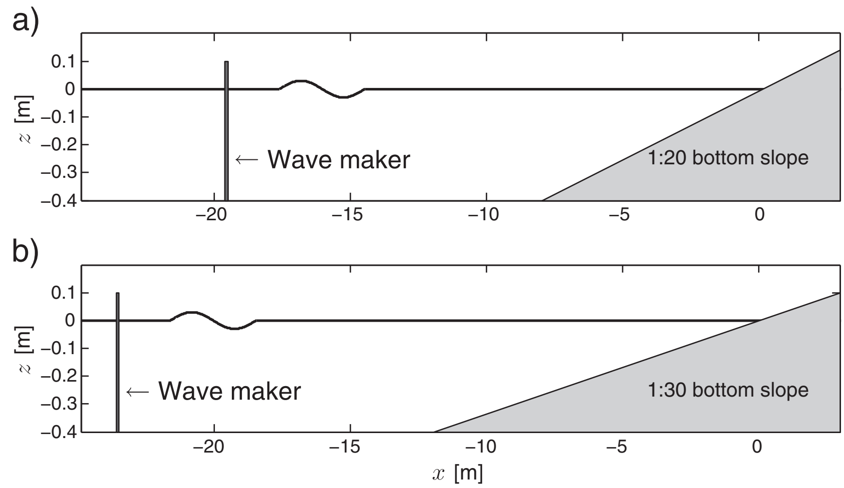

Fig. 1. Numerical wave flume. a) 1-case, bottom slope = 1:20; b) 2-cases, bottom slope = 1:30.

which f_p denotes the peak frequency of the incident wave spectrum. Note that the short-wave horizontal velocity component, u_w, is obtained by subtracting the low-frequency volume flux divided by depth from the total horizontal velocity in accordance with Mei (1989). The separation of Mei (1989) is preferred here to that proposed by Phillips (1977) since the former avoids the extrapolation, with the corresponding uncertainties, of the current, U, and the short-wave velocities, u_w, above the trough level where water is only intermittently present and neither the average nor the filter operator are uniquely defined there. Moreover, it is worth mentioning that the adoption of the separation technique proposed by Mei (1989) leads to a definition of the radiation stress that is equivalent to that proposed by Phillips (1977), as demonstrated by Svendsen (2005).

The depth-integrated energy equation for statistically steady low-frequency waves states that, if the dissipative processes are negligible, the rate of work done by the radiation stress is in balance with the long-wave energy flux gradient:

$$\frac{\partial \overline{W}}{\partial x} + \overline{U \frac{\partial S_{xx}}{\partial x}} = 0 \tag{3}$$

where the overline denotes integrating over a time period sufficiently long to ensure the steadiness of the low-frequency motion. W and S_{xx} are, respectively, the low-frequency energy flux and the radiation stress, defined as (see Schäffer, 1993)

$$W = U(h+\eta_c)\left(\frac{1}{2}\rho U^2 + \rho g \eta_c\right) \tag{4}$$

$$S_{xx} = \left\| \int_{-h}^{\eta} \rho\left(u_w^2 - w_w^2\right) dz \right\|_{(lf)} + \frac{1}{2}\rho g \left\| \eta_w^2 \right\|_{(lf)} \tag{5}$$

in which g is the gravitational acceleration and ρ is the fluid density. In the calculation of the radiation stress, the main contribution to the low-frequency part of the dynamic pressure comes from the vertical momentum flux of the organized part of the motion. This is in accordance with the laboratory experiments of Ting and Kirby (1994) who found that the normal turbulent stresses are small even inside the surf zone,

$$\left\| \int_{-h}^{\eta} (p - \rho g(\eta - z)) dz \right\|_{(lf)} \approx \left\| \int_{-h}^{\eta} -\rho w_w^2 dz \right\|_{(lf)} \tag{6}$$

The pressure, S_p, and momentum, S_m, contributions of the radiation stress are defined as:

$$S_p = \left\| \int_{-h}^{\eta} -\rho w_w^2 dz \right\|_{(lf)} + \frac{1}{2}\rho g \left\| \eta_w^2 \right\|_{(lf)} \tag{7}$$

$$S_m = \left\| \int_{-h}^{\eta} \rho u_w^2 dz \right\|_{(lf)} \tag{8}$$

3.2. Separation of long waves over the horizontal bottom

Infragravity motions observed on continental shelves are a mixture of forced waves, which are phase-coupled to swell and sea, and uncoupled free waves radiated from shore or arriving from remote sources (Herbers et al., 1995a). In the cross-shore direction, the total infragravity motion can be separated as:

$$\eta_c = \eta_b + \eta_f^+ + \eta_f^- \tag{9}$$

$$U = U_b + U_f^+ + U_f^- \tag{10}$$

in which the subscripts b and f stand for bound and free waves and the superscripts + and - indicate shoreward- and seaward-directed components. In this study, the separation of the total infragravity motion into bound and free waves is conducted over the horizontal bottom region of the flume. The total bound waves are obtained as a linear sum of the bound-wave contributions of each possible pair of primary-wave components. The surface level of the incident bound wave $\eta_{b(i,j)}$ generated by the difference interactions between two short-wave components (i, j) is calculated from the formulation of Longuet-Higgins and Stewart (1962):

$$\eta_{b(i,j)} = -\frac{S_{xx(i,j)} - C_{(i,j)}}{\rho\left(gh - c_{g(i,j)}^2\right)} \tag{11}$$

where the subscripts distinguish between the wave components, c_g denotes the group celerity, $S_{xx(i,j)}$ is the radiation stress delivered by

Table 1
Geometrical parameters.

Study	h_0 [m]	h_x	MR generation (Δx, Δz) [cm]	MR swash (Δx, Δz) [cm]	I_r
L11	0.4	1:25	(1.2, 0.5)	(0.8, 0.5)	0.21÷0.44
PW	0.4	1:20÷1:30	(1.2, 0.5)	(0.8, 0.5)	0.21÷0.43

the two components and $C_{(i,j)}$ is an integration constant. To the lowest order of approximation $S_{xx(i,j)}$ can be written as:

$$S_{xx(i,j)} = \frac{1}{2}\rho g A_{(i,j)}^2 \left(\frac{2c_{g(i,j)}}{c} - \frac{1}{2}\right) \tag{12}$$

where $A_{(i,j)}^2$ is the contribution of the two wave components to the squared modulation of a short-wave system constituted by N wave components:

$$A_{(i,j)}^2 = a_i^2 \left(\frac{1}{N-1} + \frac{a_j^2}{(N-1)a_i^2} + 2\frac{a_j}{a_i}\cos\left(\psi_j - \psi_i\right)\right) \tag{13}$$

in which a and ψ are the wave amplitude and the phase angle, respectively. Eq. (13) reduces to Eq. (2.33) of Schäffer (1993) for a short-wave system constituted by only 2 components. Imposing that the mean bound-wave free surface must be zero when averaged over a time period much longer than the group period yields:

$$C_{(i,j)} = \frac{1}{2}\rho g a_i^2 \left(\frac{1}{N-1} + \frac{a_j^2}{(N-1)a_i^2}\right)\left(\frac{2c_{g(i,j)}}{c} - \frac{1}{2}\right) \tag{14}$$

The horizontal velocity U_b of bound waves follows from continuity:

$$U_{b(i,j)} = \frac{\eta_{b(i,j)} c_{g(i,j)}}{h} \tag{15}$$

The total free surface level η_b and horizontal velocity U_b of bound waves related by a primary-wave system composed by N components is given by the sum of the interactions resulting from each pair of wave components:

$$\eta_b = \sum_{i=1}^{N-1} \sum_{j=i+1}^{N} \eta_{b(i,j)} \tag{16}$$

$$U_b = \sum_{i=1}^{N-1} \sum_{j=i+1}^{N} U_{b(i,j)} \tag{17}$$

Once the incident bound motion has been calculated, it is subtracted from the total long waves obtaining a low-frequency motion composed by free long waves only:

$$\eta_f = \eta_c - \eta_b \tag{18}$$

$$U_f = U - U_b \tag{19}$$

The signal is then separated into incident and outgoing free long waves using the colocated method of Guza et al. (1984):

$$\eta_f^{\pm} = \frac{\eta_f \pm U_f\sqrt{h/g}}{2} \tag{20}$$

$$U_f^{\pm} = \pm\frac{c\eta_f^{\pm}}{h} \tag{21}$$

3.3. Separation of long waves over the sloping bottom

The separation between incident bound, incident free and outgoing free waves presented in Section 3.2 is not applicable over the sloping bottom since an analytical solution for incident bound waves is not known there. In fact, as pointed out by Baldock (2006), no rigorous separation procedure exists for irregular waves breaking over a sloping bottom. Nevertheless, many studies have successfully discriminated between incident and outgoing waves in their infragravity-wave analysis demonstrating that the proposed separation procedures provide reliable quantitative results (see for example Battjes et al., 2004; Elgar and Guza, 1985; Sheremet et al., 2002).

In this work, the shoreward and seaward components of the low-frequency motion are decomposed applying the approach developed by Guza et al. (1984) and successively modified by van Dongeren (1997) to account for the fact that the incoming waves are predominantly forced and are thus propagating with the group celerity. The incoming and outgoing components of the low frequency free surface elevation and horizontal velocity are calculated as:

$$\eta_c^{\pm} = \frac{c(\eta_c - \overline{\eta_c}) \pm (h + \overline{\eta_c})U}{c_g + c} \tag{22}$$

$$U^{\pm} = \pm\frac{c_g \eta_c^{\pm}}{h + \overline{\eta_c}} \tag{23}$$

where the overline denotes the time integration over the entire time series, $\overline{\eta_c}$ represents the steady set-up, $c = \sqrt{g(h + \overline{\eta_c})}$ is the free long-wave celerity and c_g is the group celerity set equal to the linear group celerity of the primary waves at the peak frequency.

4. Results

In this section we present the analysis of ten irregular wave cases simulated with the IH-2VOF model. Special attention is devoted to the analysis of the long-wave component. The simulations are carried out with the wave flume geometry and numerical mesh described in Section 2.2. The present analysis is extended up to the shoreward limit of the surf zone where $h+\eta>0$ at every time instant coinciding with the land-most location that is always wet. Therefore, the swash zone, defined as the region where water alternatively covers and uncovers the beach face, is not analyzed and its effects are taken into account globally by calculating the reflection coefficient at the shoreward limit of the surf zone (see Section 4.5).

4.1. Wave generation

Ten random-wave numerical simulations with varying significant wave height H_s and bottom slope h_x are carried out. The frequencies f_1 and f_N specify the lower and upper limits for the primary-wave band which is divided into a high number N (in the order of 100) of equal increments Δf. Successively, a random selection over each increment provides the discrete frequency sequence of the primary components. The Fourier amplitudes are specified in order to match a JONSWAP spectrum with enhancement factor γ of 3.3. Finally, the phase sequence is randomly selected from a uniform distribution over the range 0 and 2π.

The same phase and frequency sequences are used in order to conserve the structure of the wave groups (Baldock and Huntley, 2002). The boundary conditions for the numerical model are provided by a second order wave control signal (Barthel et al., 1983) with active wave absorption in order to reproduce the long bound waves minimizing the spurious free long waves generated and reflected at the wave maker, see Lara et al. (2011). Each experiment is 350 s long. The data from the first 60 s are not included in the following analyses in order to allow waves and mean currents to reach a quasi steady state. Table 2 summarizes the ten cases with the corresponding Iribarren number I_r and peak frequency f_p.

4.2. Nonlinear interactions in constant depth

Here we present an analysis of the nonliner interactions in the region of the numerical flume characterized by a horizontal bottom with special emphasis on free long waves in order to check the

Table 2
Simulated wave cases.

Case	h_x	f_1 [Hz]	f_N [Hz]	f_p [Hz]	H_s [m]	I_r
1-A	1:20	0.5	0.9	0.65	0.05	0.43
1-B	1:20	0.5	0.9	0.65	0.06	0.39
1-C	1:20	0.5	0.9	0.65	0.07	0.36
1-D	1:20	0.5	0.9	0.65	0.08	0.34
1-E	1:20	0.5	0.9	0.65	0.09	0.32
2-A	1:30	0.5	0.9	0.65	0.05	0.29
2-B	1:30	0.5	0.9	0.65	0.06	0.26
2-C	1:30	0.5	0.9	0.65	0.07	0.24
2-D	1:30	0.5	0.9	0.65	0.08	0.23
2-E	1:30	0.5	0.9	0.65	0.09	0.21

generation and absorption boundary conditions. The energy spectra for case 1-A in the constant-depth region of the flume are plotted in Fig. 2. The spectral estimates, obtained from Fourier transforms of a time series of 256 s sampled at 16 Hz, are smoothed by merging 3 frequency bands leading to a final resolution of 0.0117 Hz. The dashed line denotes the energy spectrum obtained from the numerical simulation, while the light solid line is the theoretical second order spectrum calculated from the formulation of Longuet-Higgins and Stewart (1960). The superharmonic ($2f_1<f<2f_N$) and subharmonic ($\Delta f<f<f_N-f_1$) bands arise, respectively, as a result of sum and difference interactions between the primary-wave components. The simulated data are in excellent agreement with the superharmonic band of the theoretical spectra and the small energy excess just above the upper limit of the primary frequency band ($f_N<f<2f_1$) seems to be attributable to higher-order interactions not predicted by the second order theory (Freilich and Guza, 1984). On the other hand, the simulated low-frequency band shows significant discrepancies from the theoretical spectra, as expected. This mismatch is more evident near the upper limit of the subharmonic band and is likely to be due to free long waves not predicted by the theoretical formulation.

Classical surf beat theories take into account a long-wave field outside the surf zone composed only by incident bound waves and outgoing free long waves generated in the surf zone and (or) reflected by the sloping bottom (Longuet-Higgins and Stewart, 1962; Symonds et al., 1982). Therefore, minimum incident free long-wave energy levels are desirable in the generation region of laboratory and numerical studies, being an indicator of the high effectiveness of generation and absorption algorithms. In this work the different long-wave modes are separated in the constant depth region of the flume using the procedure described in Section 3.2. It is worth mentioning that the procedure of Section 3.2 strictly applies to shallow water waves. In 0.4 m depth, linear theory states that the shallow water wave condition ($kh<\pi/10$) is satisfied for waves at frequencies lower than 0.25 Hz. Therefore, the high-frequency tail ($0.25<f<0.325$ Hz) of the low-frequency band lies outside the shallow water regime. However, due to the relatively low values of the relative water depth ($kh\leq 1/7.5$ for $f\leq 0.325$ Hz) and the low energy contained in the frequency band $0.25<f<0.325$ Hz with respect to the total low-frequency energy (see Fig. 3), we extend the analysis to the entire low-frequency domain.

Fig. 3 shows the comparisons between the incident and outgoing low-frequency free surface energy spectra in the constant depth region of the flume. Energy levels of both incident and outgoing free waves are much lower than those of the bound long waves for the lower band ($f<0.08$ Hz) of the subharmonic frequencies suggesting that the lowest frequency motion is principally dominated by bound waves in the constant depth region of the flume. Furthermore, incident free long waves show small energy levels over the entire low-frequency domain consistent with a minimum free long-wave generation and a high absorption at the wave maker.

Thus, the separation between long-wave modes in the constant depth region points out that the excess of low-frequency energy in the numerical model with respect to the theoretical formulation is almost totally attributable to free outgoing long waves generated over the sloping bottom. The small values of low-frequency incident free energy levels attest the high accuracy of the generation and the absorption algorithms implemented in the model.

4.3. Radiation stress evolution

In laboratory wave flume experiments, the cross-shore evolution of the mean radiation stress is usually estimated from the mean water level information (Svendsen and Putrevu, 1993). Laboratory experiments reporting a complete derivation of the radiation stress obtained from velocity and free surface displacement fields are scarce and only provide results at a limited number of locations (Stive and Wind, 1982). By means of RANS numerical simulations, Torres-Freyermuth et al. (2007) provide a rigorous evaluation of the radiation stress. In that study the time average carried out within an interval of several wave periods for irregular waves yields to the calculation only of the mean radiation stress and thus omits the slow oscillations in time. In this work, the use of the low-pass filter preserves the time dependence of the radiation stress and allows evaluating the nonlinear term $\overline{\frac{\partial S_{xx}}{\partial x} U}$ involved in the energy balance Eq. (3). Moreover, the high spatial resolution provided by the model makes it possible to use a quasi-continuous presentation of the radiation stress cross-shore evolution.

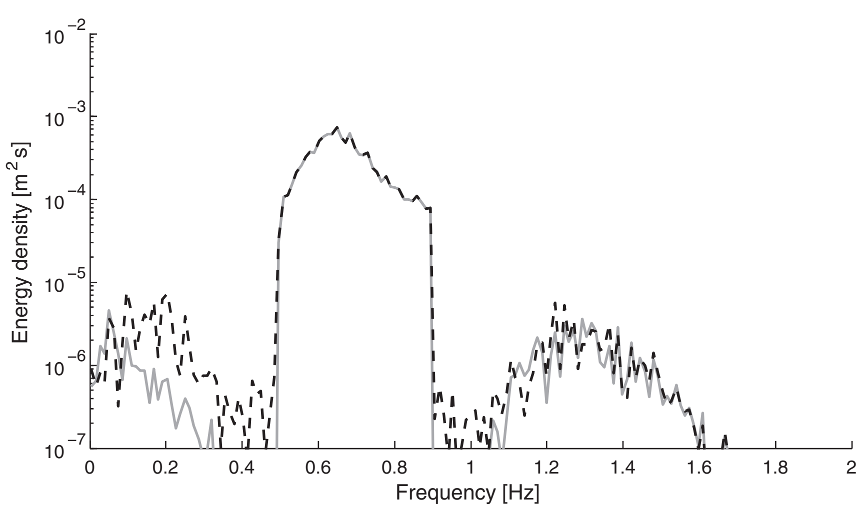

Fig. 2. Energy spectra over the horizontal bottom, case 1-A. Solid line: second order theory; dashed line: simulated.

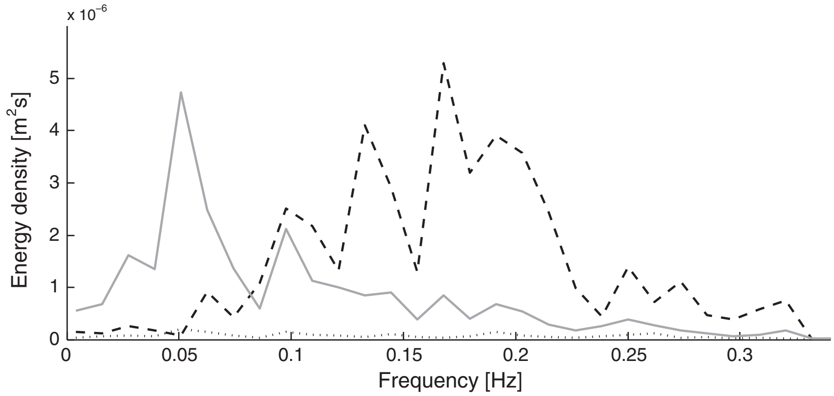

Fig. 3. Low-frequency energy spectra, case 1-A. Solid line: incident bound; dashed line: outgoing free; dotted line: incident free.

Figs. 4 and 5 show the mean radiation stress $\overline{S_{xx}}$ variation over the sloping bottom for cases 1-A and 1-E which are characterized by plunging and spilling breaking, respectively. Moreover, the cross-shore variation of the root mean square wave height H_{rms} is displayed in the upper panel of both figures. In this work, the overline denotes time averaging over the entire time series, excluding the first 60 s in order to avoid start-up effects. The total $\overline{S_{xx}}$, the pressure contribution $\overline{S_p}$, Eq. (7), and the momentum contribution $\overline{S_m}$, Eq. (8), are illustrated. The total radiation stress is enhanced in the shoaling zone as a result of the increasing H_{rms}. The maximum radiation stress is located close to the breakpoint x_b, defined as the point where the higher value of H_{rms} is observed. This is in accordance with the regular wave experiments of Stive and Wind (1982). In the outer surf zone the radiation stress starts to decrease showing mild negative gradients between x_b and x_o. Here x_o is defined as the point where $(H_{rms}/H_{rms0})^2 = 0.75$, H_{rms0} being the offshore root mean square wave height. Note that considering the wave energy directly proportional to H_{rms}^2, it is possible to state that a quarter of the offshore incident wave energy is dissipated between x_b and x_o. In this work, the zone between x_b and x_o is what we refer to as the outer surf zone. Shoreward of x_o the largest negative radiation stress gradients are observed. Case 1-A, see Fig. 4, shows a weak variation of the momentum part seaward of x_o consistent with the conversion of a significant amount of potential energy into kinetic energy during the breaking process (Svendsen, 2005). On the other hand, the pressure part strongly decreases in conjunction with the damping of wave amplitude. As a result of the different trends of the two contributions, well inside the surf zone the momentum part overcomes the pressure part and can constitute up to the 85% of the total radiation stress. The other simulated cases present a ratio between the momentum part and the total radiation stress which ranges between 0.8 and 0.85 well inside the surf zone. Linear wave theory predicts a ratio of the momentum part to the total radiation stress equal to 2/3, while the theoretical approximation of Svendsen (2005) for sawtooth shape waves including the roller brings a ratio of 0.8 which is in closer agreement with these numerical results. Case 1-E, characterized by a relatively low Iribarren number, shows similar features but with weaker gradients inside a broader surf zone. Analysis of cases characterized by a milder h_x do not introduce significant additional insights.

4.4. Energy balance

Many laboratory studies dealing with infragravity waves inferred the forcing of the long waves from the short-wave envelope (Baldock and Huntley, 2002; Battjes et al., 2004; Janssen et al., 2003) as a consequence of the lack of the sufficiently detailed velocity field measurements required to calculate the radiation stress. The calculation of the envelope is straightforward and allows direct identification of the relationship between the wave groups and the long waves. However, significant uncertainties can arise inside the surf zone where the short-wave envelope is poorly defined (Sobey and Liang, 1986). Battjes et al. (2004) carried out an energy balance analysis limited to the shoaling zone since they calculated the nonlinear energy transfer term neglecting the gradient of the amplitude of the radiation stress considering its contribution much smaller than that of the spatial phase variation. This assumption, as already pointed out by Battjes et al. (2004) themselves, breaks down in the surf zone where strong radiation stress gradients

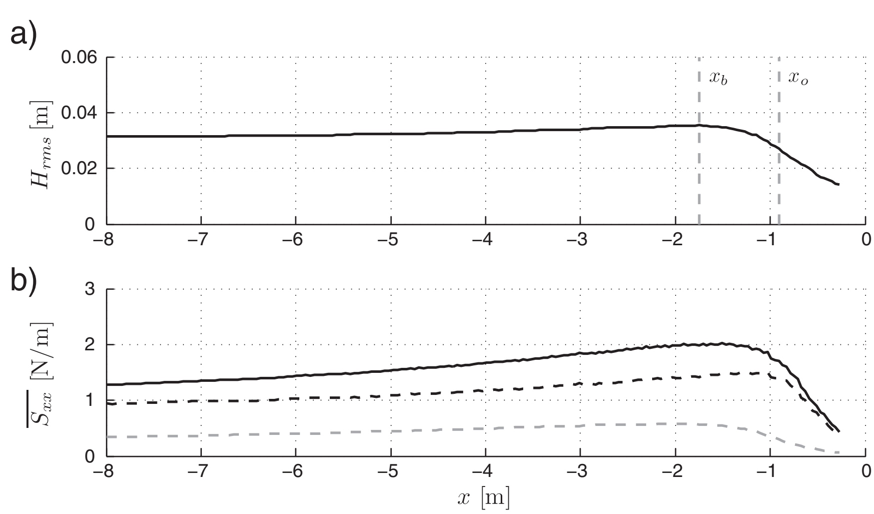

Fig. 4. Cross-shore evolution of H_{rms} and $\overline{S_{xx}}$, case 1-A. a) H_{rms}; b) solid line: total radiation stress $\overline{S_{xx}}$, dark dashed line: momentum part $\overline{S_m}$, light dashed line: pressure part $\overline{S_p}$.

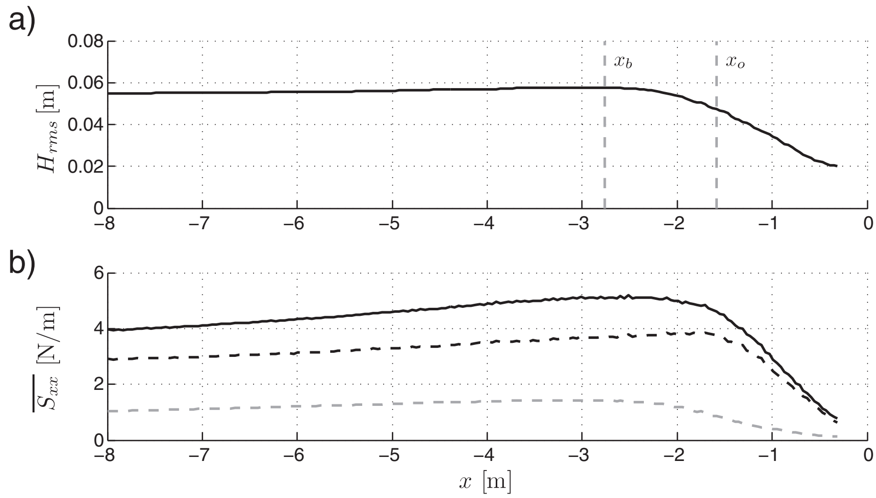

Fig. 5. Cross-shore evolution of H_{rms} and $\overline{S_{xx}}$, case 1-E. a) H_{rms}; b) solid line: total radiation stress $\overline{S_{xx}}$, dark dashed line: momentum part $\overline{S_m}$, light dashed line: pressure part $\overline{S_p}$.

occur (see Figs. 4 and 5). In this work, no assumptions are involved in the radiation stress calculation and the energy transfer analysis is extended within the surf zone.

A cross-correlation analysis is conducted here to find out the relationship between the forcing and the low frequency motion. The normalized cross-correlation function between two time series $a(t)$ and $b(t)$ is defined as:

$$C_{ab}(\tau) = \frac{\overline{a(t)b(t+\tau)}}{\sigma_a \sigma b} \tag{24}$$

where τ is the time shift, σ_a and σ_b are the standard deviations of the two time series, and the overline denotes time averaging over the time series length. Fig. 6a illustrates the cross-correlation between the low-frequency free surface displacement η_c and the radiation stress S_{xx} measured at the same location for case 1-E. In Fig. 6b we show the result of cross-correlating the low frequency horizontal velocity U with the radiation stress S_{xx} measured at the same location, for the same case. Near the toe of the beach ($x=-8$ m), the strong negative correlations at zero time lag shown in Fig. 6a as well as in Fig. 6b are in accordance with the solution of Longuet-Higgins and Stewart (1962) indicating that the local forcing drives the incident long-wave motion. As waves propagate over the sloping bottom, shoreward increasing positive time lags reveal a delay of the low-frequency motion with respect to the forcing suggesting that the long-wave evolution induced by the bottom slope becomes significant. The positive correlation for small negative time lags is consistent with a positive surge propagating in front of the group constituted by the positive part of the long bound wave (Baldock, 2006) and free long waves radiated shoreward as short waves shoal in intermediate water (Lara et al., 2011; Nielsen and Baldock, 2010). Inside the surf zone, for $x>-1.5$ m, Fig. 6a shows the positive correlation ridge passing from negative values to zero lag as reported by previous studies (Janssen et al., 2003; Torres-Freyermuth et al., 2010). The gradual change suggests that the short waves in front of the group reach the positive surge and propagate above a long-wave crest experiencing a positive current as can be inferred from Fig. 6b. The observation of Fig. 6a and b indicates that the short-wave energy dissipation is delayed as a consequence of the positive current and the temporarily increased water depth. Thus, the highest broken waves are likely to approach the moving shoreline when it is displaced shoreward with respect to its mean position. This has an important effect on run-up oscillations and, consequently, on dune erosion and damages to structures (Kamphuis, 1996). On the other hand, the long-wave trough enhances the breaking of the short waves in the rear part of the groups which propagate with difficulty inside the surf zone. A weak negative correlation due to the reflection at the shoreline of the long wave trough is observed in Fig. 6a along the white dashed line which indicates the travel time required for wave groups to reach the shore and for long waves to travel back to the specified location. The mathematical expression of the predicted travel time is:

$$F(\tau, x) = \int_x^0 \left(\frac{1}{c_g} + \frac{1}{c}\right) dx - \tau = 0 \tag{25}$$

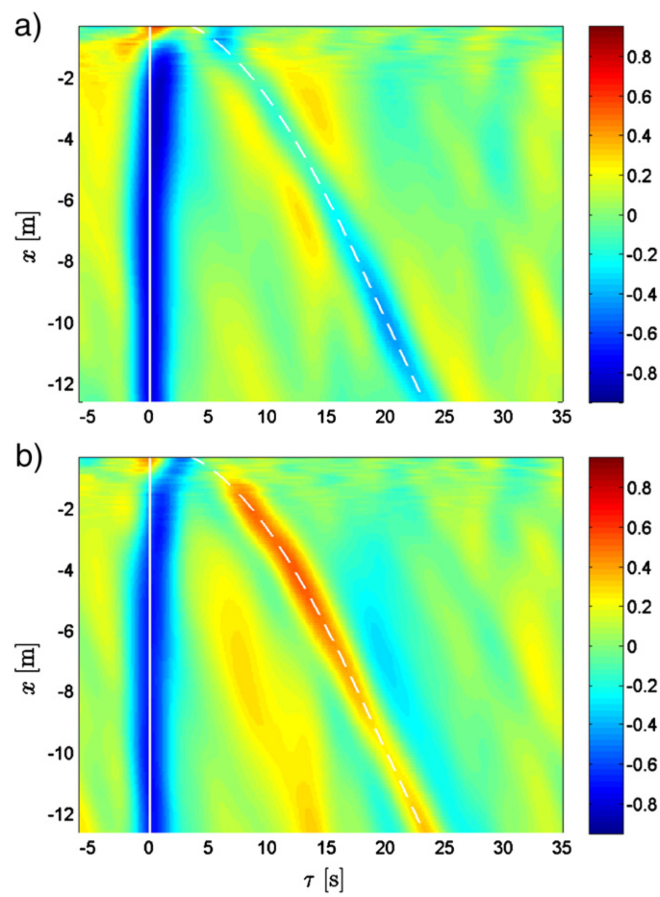

Fig. 6. Cross-correlation between low-frequency motion and radiation stress, case 1-E. a) cross-correlation between low-frequency free surface displacement and radiation stress, b) cross-correlation between low-frequency horizontal velocity and radiation stress. The dashed white line indicates summed travel times determined from the wave celerity.

The reflection at the shoreline of the positive surge results in a weak positive correlation for positive time lags. Moreover, Fig. 6a does not reveal a clear presence of significant breakpoint-generated long waves whereas the positive ridge of Fig. 6b is consistent with low-frequency currents associated with long waves radiated directly seaward from the breaking zone. Baldock and Huntley (2002) suggested that the breakpoint generation becomes ineffective for large values of the normalized surf zone width parameter χ (Symonds et al., 1982). An equivalent criterion was later provided by Battjes et al. (2004) who found that bound waves overcome breakpoint generated waves for $\beta_s<0.3$. β_s is the normalized bed slope parameters defined as:

$$\beta_s = \frac{h_x}{\omega}\sqrt{\frac{g}{h}} \tag{26}$$

Taking $h=0.25$ m as a representative depth in the shoaling zone and $\omega=2\pi f_p/4$, we find $\beta_s\approx0.3$ for case 1-E suggesting that breakpoint generated waves are not negligible (Battjes et al., 2004). The fact that breakpoint-generated long waves are hardly detectable in Fig. 6a while their significance is clear in Fig. 6b seems to be strictly related to the transient nature of this type of waves. Furthermore, interaction with long waves reflected from the shoreline can play a role as well. In this work, we avoid going into the details of the mechanics of breakpoint-forced long waves. In fact, the main purpose of the cross-correlation analysis presented in this section is to study the relationship between the total low-frequency motion and the forcing inside the surf zone and a separation between bound-released and breakpoint-generated long waves is beyond the scope of this paper.

Figs. 7 and 8 show the terms directly involved in the energy balance Eq. (3) versus cross-shore distance for cases 1-E and 2-E, respectively. The mean low frequency energy flux, $\bar{W}$, takes positive values at the toe of the beach ($x=-8$ m), as seen in Fig. 7a. Note that $\bar{W}$ is the net energy flux constituted by the positive flux carried by incoming waves and the negative flux carried by outgoing waves. Thus, positive values of $\bar{W}$ are consistent with a long-wave motion dominated by incident waves. On the other hand, cases characterized by lower incident swell energy show negative $\bar{W}$ values at the toe of the beach, suggesting that seaward-propagating long waves overcome shoreward-propagating long waves in this region (see Section 4.5). For case 1-E, over the sloping bottom, the net energy flux is enhanced as waves approach breaking; also in the outer surf zone, it continues to increase with the maximum values observed close to the point x_o. Hence, the ratio between incident and outgoing long waves attains an absolute maximum in the outer surf zone in accordance with the results obtained through bispectral analysis by Ruessink (1998). Well inside the surf zone, the energy flux is damped out as a result of dissipation processes which appear important there. In this paper, the term low-frequency energy dissipation is used to denote both energy transfer to other frequency bands and mechanical energy conversion into other forms. At the shoreward limit of the surf zone for case 1-E, the energy flux tends to relatively small positive values (on the same order of those observed at the toe of the beach). Long wave dissipation due to swash processes thus appears weak in case 1-E. This implies a high, although lower than unity, reflection coefficient (see Section 4.5) for low frequency motion at the shoreward limit of the surf zone as observed by Sheremet et al. (2002).

In order to analyze the role played by the interactions with the swell field in the enhancement and dissipation of the low frequency energy flux, the rate of work done by the radiation stress (the nonlinear energy transfer term $\overline{\frac{\partial S_{xx}}{\partial x}U}$) and the energy flux gradient $\frac{\partial \overline{W}}{\partial x}$ are compared in Fig. 7b. In the shoaling zone the nonlinear energy transfer term balances the positive energy flux gradient, consistent with an energy transfer from short to long waves as a result of the work done by the radiation stress. Even in the outer surf zone ($x_b<x<x_o$), where the maximum energy transfer rate is observed, the positive energy flux gradients are in balance with the nonlinear energy transfer term. Just shoreward of x_o the nonlinear energy transfer term roughly matches the energy flux gradient which passes from positive to negative values. Thus, the dissipation of long-wave energy observed in the middle surf zone appears to arise as a result of an inverted energy transfer with infragravity waves transferring energy back to short waves. A negative infragravity energy flux gradient balanced by the nonlinear energy transfer term was already observed in the field experiments of Thomson et al. (2006) and Henderson et al. (2006). However, in contrast with the present results, Henderson et al. (2006) reported a dissipation of the infragravity waves starting outside the surf zone. For the cases presented here, the inversion of energy transfer occurs in the middle surf zone, just shoreward of x_o where strong radiation stress gradients due to short-wave breaking are observed (see Figs. 4 and 5). In the inner surf zone the energy transfer term tends to decrease due to the strong reduction of the radiation stress which becomes unable to drive the long-wave motion. On the other hand, dissipation of infragravity energy is still present as attested by the negative gradients of the energy flux. This pattern suggests that the interaction with the swell field can hardly be responsible for the infragravity energy loss in the most shoreward part of the surf zone. The energy balance analysis for case 2-E (Fig. 8) and the other simulated cases (not shown) brings analogous results.

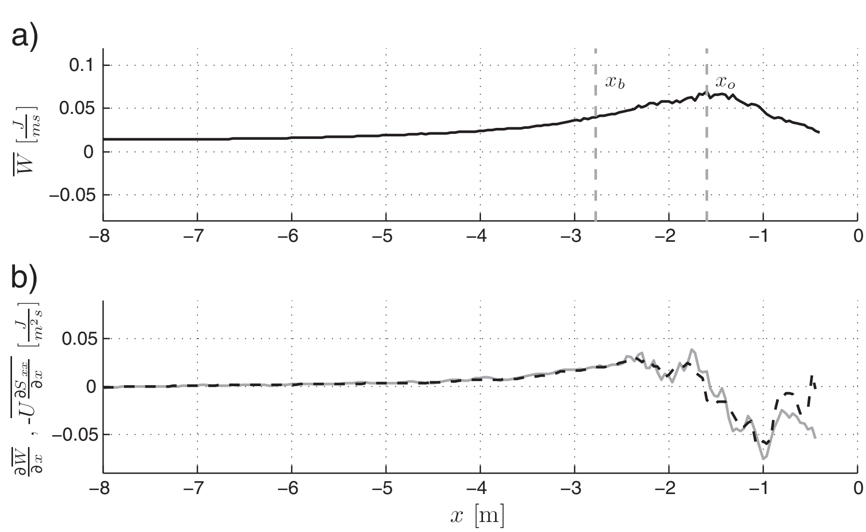

Fig. 7. Cross-shore evolution of a) mean energy flux and b) solid line: mean energy flux gradient, dashed line: rate of work done by the radiation stress. Case 1-E.

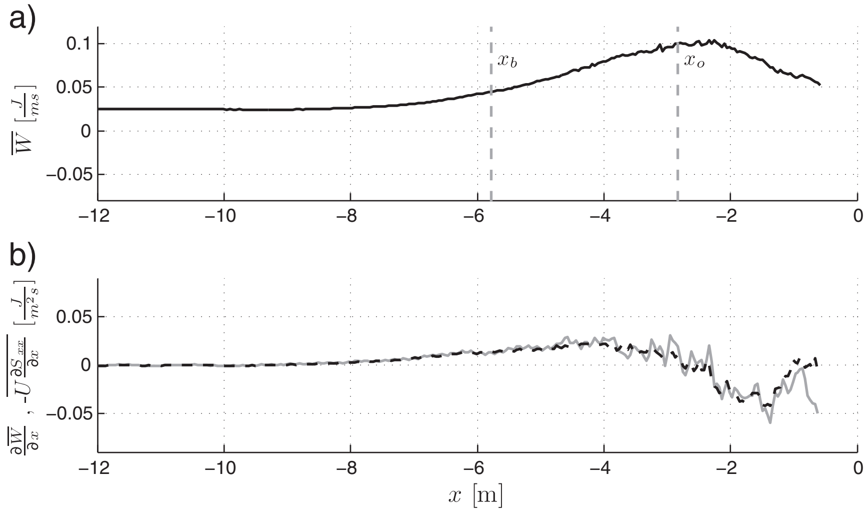

Fig. 8. Cross-shore evolution of a) mean energy flux and b) solid line: mean energy flux gradient, dashed line: rate of work done by the radiation stress. Case 2-E.

4.5. Energy dissipation at the shoreline

The results shown in Section 4.4 are obtained without the necessity to discriminate between seaward and shoreward components of the low-frequency motion. In this section, we present the results of the separation procedure described in Section 3.3 in order to quantitatively evaluate the energy dissipation in the inner surf zone and the reflection coefficient at the shoreline.

The separation procedure allows analyzing the seaward and shoreward components of the low-frequency energy flux, see Fig. 9 where cases 1-A and 1-E are represented. The incident energy flux is strongly enhanced up to the breakpoint and within the outer surf zone where it reaches its maximum values. Then, it decreases implying an infragravity energy loss inside the surf zone which appears more marked for energetic wave cases. The seaward energy flux resulting from the long wave reflection at the shoreline seems to suffer an energy loss inside the surf zone and then a gain in the outer surf zone. Determining if these oscillations can be interpreted as a physical phenomenon or they are instead due to the separation procedure is an open issue which has been addressed in the literature (Baldock, 2009, 2011; van Dongeren et al., 2007). More seaward, in the shoaling zone the energy flux remains roughly constant suggesting a minimal energy transfer between free outgoing long waves and incident short wave groups. Fig. 9a shows that outgoing free waves dominate the low frequency motion at the toe of the beach for case 1-A, while for the more energetic sea state of case 1-E (see Fig. 9b), the incident long waves overcome the outgoing free waves in accordance with a positive net energy flux already observed in Fig. 7a. This is in agreement with Herbers et al. (1995a) who observed an increasing relative contribution of incident (predominantly forced) waves to the infragravity band energy with both increasing swell energy and decreasing water depth. At a specified location, the low-frequency motion can be dominated by incident or outgoing waves as a result of the different energy gains and losses occurring shoreward of the specified position and is strictly related with the development of free long waves which depend on the entire bottom profile (Herbers et al., 1995b). In fact, smaller short waves are allowed to propagate without breaking into shallower waters enabling a stronger energy transfer to long waves. As a result, the infragravity energy gain shoreward of the considered location exceeds dissipation inside the surf zone. The opposite occurs for long waves generated during energetic state cases which experience a relatively weak energy transfer from short waves in the shoaling zone and a strong dissipation inside the surf zone.

Here, we study the shoreline infragravity energy dissipation by comparing the incident and the outgoing long wave amplitudes at the shoreward limit of the surf zone. van Dongeren et al. (2007) found that the relationship between the reflection coefficient, R, and the surf beat similarity parameter β_H, originally proposed by Battjes (1974) for short waves, can also be applied to long waves. Here, we

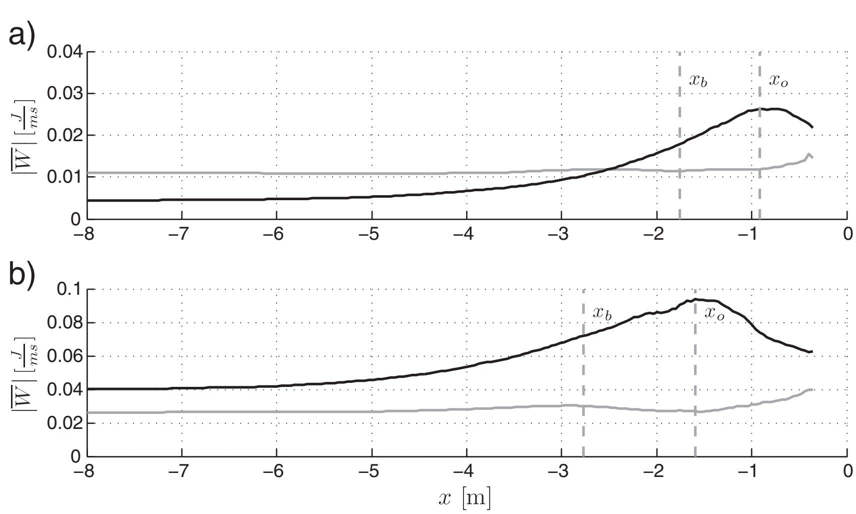

Fig. 9. Cross-shore evolution of absolute values of shoreward (dark line) and seaward (light line) low frequency energy flux. a) Case 1-A; b) case 1-E.

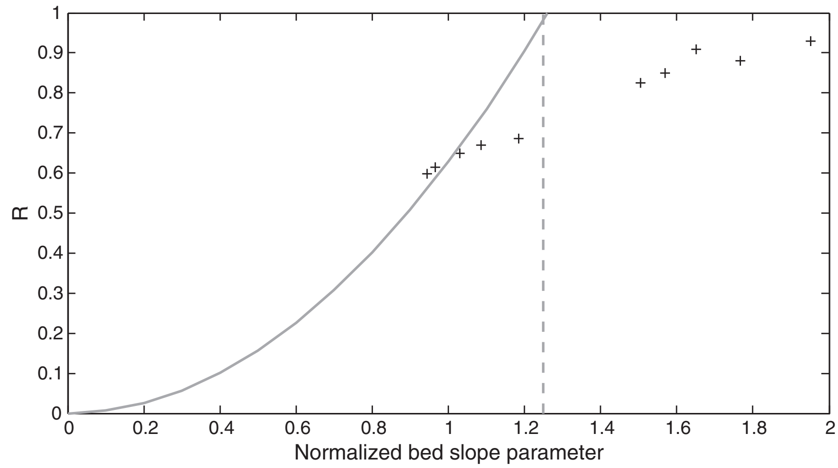

Fig. 10. Reflection coefficient versus normalized bed slope parameter. Solid line: Battjes (1974) relationship, dashed line: $\beta_H = 1.25$.

adopt an analogous procedure in order to investigate the infragravity energy dissipation in the swash zone. The normalized slope parameter and the reflection coefficient are defined as:

$$\beta_H = \frac{h_x}{\omega}\sqrt{\frac{g}{H^+}} \tag{27}$$

$$R = \frac{H^-}{H^+} \tag{28}$$

in which ω is the long wave radian frequency, h_x is the bed slope and H^+ and H^- are the root mean square height of the incoming and outgoing long waves, respectively. In the ω definition we use the central frequency of the low frequency range. Fig. 10 shows the reflection coefficient plotted against the normalized bed slope parameter β_H. The solid line indicates the relationship proposed by Battjes (1974): $R = 0.2\pi\beta_H^2$. For β_H higher than 1.25 the reflection coefficient tends to values in the order of 0.9, consistent with small low-frequency energy dissipation inside the swash zone. For cases characterized by a $\beta_H < 1.25$ (dashed vertical line) the reflection coefficient seems to be well predicted by the Battjes (1974) relationship, although with a sensible scatter, confirming the numerical results obtained by van Dongeren et al. (2007). Therefore, for cases characterized by low β_H, it appears that the swash zone processes cause significant infragravity energy dissipation.

Finally, we investigate the infragravity energy damping in the inner surf zone where the negative low frequency energy flux gradients are not in balance with the rate of work done by the radiation stress. van Dongeren et al. (2007) estimated the rate of energy dissipation by breaking and bottom friction using, respectively, the formulations proposed by Battjes and Janssen (1978) and Henderson and Bowen (2002). In agreement with the field investigations of Henderson et al. (2006), they found that bottom friction leads to small dissipation rates and concluded that it cannot be considered the main agent for energy dissipation inside the surf zone. On the other hand, they attributed the energy dissipation to self–self interactions between low-frequency components leading to the steepening of the long-wave front and eventually to long wave breaking in shallow waters. Fig. 11 shows the cross-shore evolution of the δ parameter, defined as the ratio between the low-frequency incident root mean square wave height and the water depth

$$\delta = \frac{H^+}{h + \overline{\eta_c}} \tag{29}$$

For the cases considered here, at the shoreward limit of the surf zone the relative height δ ranges between 0.4 and 0.6 and is thus smaller than the classical value of 0.8 considered for short-wave breaking. Thus, a rigorous application of the short-wave breaking criterion to long waves would lead to the conclusion that long-wave breaking hardly occurs. Nevertheless, values of the relative height of the order of 0.5 point out the importance of long-wave nonlinearity. In fact, self–self interactions between infragravity wave components

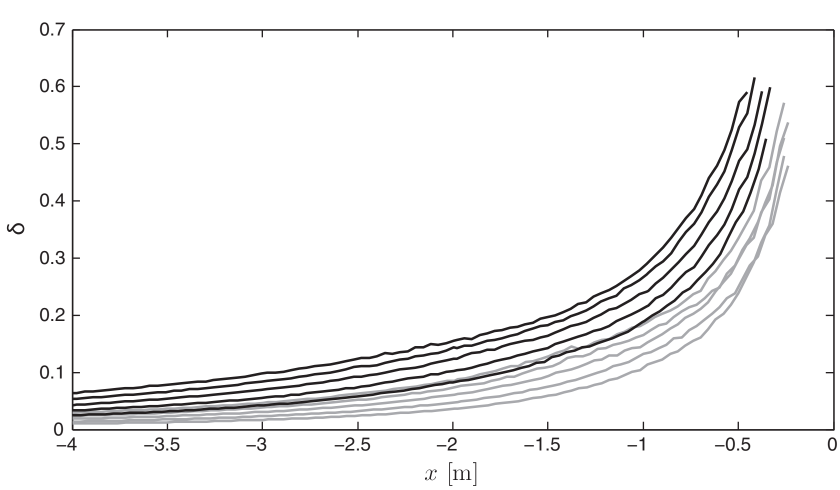

Fig. 11. Cross-shore evolution of the relative height parameter δ. Light line: 1-case; dark line: 2-cases.

appear to be sufficiently strong to allow a marked steepening of the long waves in conjunction with an energy transfer to higher frequencies. The present data do not provide a clear evidence of long-wave breaking outside the swash zone. However, the high δ values in conjunction with R much lower than unity suggest that for cases characterized by low β_H (β_H is of the order of unity for 1- cases) long-wave breaking is likely to occur inside the swash zone.

5. Conclusions

In this work a detailed analysis of the radiation stress evolution with applications to the energy transfer between short and long waves in the nearshore is conducted. Overcoming existing limitations in field and laboratory experiments, the radiation stress is obtained directly from the free surface and velocities provided by the numerical model IH-2VOF. Since no assumptions are involved in the radiation stress calculation, the energy balance analysis is extended over the shoaling and surf zone. Shoaling and breaking of irregular waves over different relatively steep slopes are considered.

Maximum values of the mean radiation stress are observed close to the breakpoint. The radiation stress remains almost constant within the outer surf zone and then experiences strong negative gradients in the middle surf zone. Well inside the surf zone the contribution of the momentum part to the total radiation stress is observed to overcome the contribution of the pressure part, consistent with the theoretical model of Svendsen (2005).

The numerical experiments show an infragravity energy flux increasing in the shoaling zone and in the outer surf zone. The rate of work done by the radiation stress is observed to balance the positive energy flux gradients consistent with a nonlinear energy transfer from swell to infragravity waves. The maximum low-frequency energy flux is detected at the shoreward limit of the outer surf where dissipation of infragravity energy starts. In the middle surf zone the energy flux gradients take negative values which are still balanced by the energy transfer term. Therefore, the present analysis points out that in the middle surf zone, where strong negative mean radiation stress gradients are observed, energy is transferred back to short waves through the work done by the radiation stress.

In the inner surf zone, the energy flux continues to decrease but minimal interactions of long waves with the swell field are observed. Long wave self–self interactions, attested by high values of the relative wave height δ, appear to play the prominent role in low-frequency damping processes at the limit between surf and swash zone. Furthermore, at the shoreward limit of the surf zone the normalized bottom slope parameter β_H appears to control the long-wave reflection at the shoreline in agreement with the work of van Dongeren et al. (2007). For cases characterized by a low normalized bottom slope parameter, reflection coefficients lower than unity suggest that a considerable amount of low-frequency energy is dissipated within the swash zone.

Acknowledgements

J.L. Lara is indebted to the M.E.C. for the funding provided in the "Ramon y Cajal" (RYC-2007-00690). The work is funded by the projects BIA2008-05462 and BIA2008-06044 of the "Ministerio de Ciencia e Innovacion" (Spain). The comments of the two reviewers are much appreciated. Giovanni Coco is thanked for encouragement and insightful discussions.

References

Baldock, T.E., 2006. Long wave generation by the shoaling and breaking of transient wave groups on a beach. Proceedings of the Royal Society of London Series A 462, 1853–1876.

Baldock, T.E., 2009. Bound wave release induced by short wave breaking — true or false? Proc. Coastal Dynamics: World Scientific edited.

Baldock, T., 2011. Dissipation of incident forced long waves in the surf zone — implications for the concept of bound wave release at short wave breaking. Coastal Engineering 60, 276–285.

Baldock, T.E., Huntley, D.A., 2002. Long-wave forcing by the breaking of random gravity waves on a beach. Proceedings of the Royal Society of London Series A 458, 2177–2201.

Baldock, T.E., Huntley, D.A., Bird, P.A.D., O'Hare, T., Bullock, G.N., 2000. Breakpoint generated surf beat induced by bichromatic wave groups. Coastal Engineering 39, 213–242.

Barthel, V., Mansard, E.P.D., Sand, S.E., Vis, F.C., 1983. Group bounded long waves in physical models. Ocean Engineering 10, 261–294.

Battjes, J.A., 1974. Surf similarity. Proceedings of the 14th International Conference on Coastal Engineering. ASCE, pp. 466–480.

Battjes, J.A., Janssen, J.P.F.M., 1978. Energy loss and set-up due to breaking of random waves. Proceedings of the 16th International Conference on Coastal Engineering. ASCE, pp. 569–587.

Battjes, J.A., Bakkenes, H.J., Janssen, T.T., van Dongeren, A.R., 2004. Shoaling of subharmonic gravity waves. Journal of Geophysical Research 109 (C18). http://dx.doi.org/10.1029/2003JC001863.

Elgar, S., Guza, R.T., 1985. Observations of bispectra of shoaling surface gravity waves. Journal of Fluid Mechanics 161, 425–448.

Freilich, M.H., Guza, R.T., 1984. Non-linear effects on shoaling surface gravity waves. Philosophical Transactions of the Royal Society of London, Series A (311), 1–41.

Guanche, R., Losada, I.J., Lara, J.L., 2009. Numerical analysis of wave loads for coastal structure stability. Coastal Engineering 56, 543–558.

Guza, R.T., Thorton, E.B., 1982. Swash oscillations on a natural beach. Journal of Geophysical Research 87 (C1), 483–491.

Guza, R.T., Thorton, E.B., Holman, R.A., 1984. Swash on steep and shallow beaches. Proceedings of the 19th International Conference on Coastal Engineering. ASCE, pp. 708–723.

Henderson, S.M., Bowen, A.J., 2002. Observations of surf beat forcing and dissipation. Journal of Geophysical Research 107 (C11). http://dx.doi.org/10.1029/2000JC000498.

Henderson, S.M., Guza, R.T., Elgar, S., Herbers, T.H.C., Bowen, A.J., 2006. Nonlinear generation and loss of infragravity wave energy. Journal of Geophysical Research 111 (C12007). http://dx.doi.org/10.1029/2006JC003539.

Herbers, T.H.C., Elgar, S., Guza, R.T., 1995a. Generation and propagation of infragravity waves. Journal of Geophysical Research 100 (C12), 24863–24872.

Herbers, T.H.C., Elgar, S., Guza, R.T., O'Reilly, W.C., 1995b. Infragravity frequency (0.005–0.05 Hz) motions on the shelf II, free waves. Journal of Physical Oceanography 25, 1063–1079.

Huntley, D.A., 1976. Long period waves on a natural beach. Journal of Geophysical Research 81, 6441–6449.

Janssen, T.T., Battjes, J.A., van Dongeren, A.R., 2003. Long waves induced by short-wave groups over a sloping bottom. Journal of Geophysical Research 108 (C8). http://dx.doi.org/10.1029/2002JC001515.

Jones, W.P., Launder, B.E., 1972. The prediction of laminarization with a two equations model of turbulence. International Journal of Heat and Mass Transfer 15, 301–314.

Kamphuis, J.W., 1996. Experiments on design wave height in shallow water. Proceedings of the 25th International Conference on Coastal Engineering. ASCE, pp. 221–232.

Lara, J.L., Losada, I.J., Guanche, R., 2008. Wave interaction with low-mound breakwaters using RANS model. Ocean Engineering 35, 1388–1400.

Lara, J.L., Ruju, A., Losada, I.J., 2011. Reynolds averaged Navier–Stokes modelling of long waves induced by a transient wave group on a beach. Proceedings of the Royal Society of London Series A 467, 1215–1242.

Lin, P., Liu, P.L.-F., 1998. A numerical study of breaking waves in the surf zone. Journal of Fluid Mechanics 359, 239–264.

Longuet-Higgins, M.S., Stewart, R.W., 1960. Changes in the form of short gravity waves on long waves and tidal currents. Journal of Fluid Mechanics 8, 565–583.

Longuet-Higgins, M.S., Stewart, R.W., 1962. Radiation stress and mass transport in gravity waves with application to surf beats. Journal of Fluid Mechanics 13, 481–504.

Losada, I.J., Lara, J.L., Guanche, R., González-Ondina, J.M., 2008. Numerical analysis of wave overtopping of high mound breakwaters. Coastal Engineering 55, 887–913.

Madsen, P.A., Sorensen, O.R., Schäffer, H.A., 1997. Surf zone dynamics simulated by a Boussinesq type model. Part II: Surf beat and swash oscillations for wave groups and irregular waves. Coastal Engineering 32, 289–319.

Mei, C.C., 1989. The applied dynamics of ocean surface waves. Vol. 1 of Advanced Series on Ocean Engineering. World Scientific, Singapore.

Munk, W.H., 1949. Surf beats. Transactions of the American Geophysical Union 30, 849–854.

Nielsen, P., Baldock, T., 2010. N-shaped surf beat understood in terms of transient forced waves. Coastal Engineering 57, 71–73.

Phillips, O.M., 1977. The Dynamics of the Upper Ocean. Cambridge University Press, New York.

Rodi, W., 1980. Turbulence Models and their Application in Hydraulics — A-State-of-the-Art Review. Int. Assoc. for Hydraul. Res., Delft, Netherlands.

Ruessink, B.G., 1998. Bound and free infragravity waves in the nearshore zone under breaking and nonbreaking conditions. Journal of Geophysical Research 103, 12795–12805.

Schäffer, H.A., 1993. Infragravity waves induced by short waves groups. Journal of Fluid Mechanics 247, 551–588.

Sheremet, A., Guza, R.T., Elgar, S., Herbers, T.H.C., 2002. Observations of nearshore infragravity waves: seaward and shoreward propagating components. Journal of Geophysical Research 107 (C8). http://dx.doi.org/10.1029/2001JC000970.

Shih, T.H., Zhu, J., Lumley, J.L., 1996. Calculation of wall-bounded complex flows and free shear flows. International Journal for Numerical Methods in Fluids 23, 1133–1144.

Sobey, R.J., Liang, H.B., 1986. Complex envelope identification of wave groups. Proceedings of the 20th International Conference on Coastal Engineering. ASCE, pp. 752–766.
Stive, M.J.F., Wind, H.G., 1982. A study of radiation stress and set-up in the nearshore region. Coastal Engineering 6, 1–25.
Svendsen, I.A., 2005. Introduction to nearshore hydrodynamics. Vol. 24 of Advanced Series on Ocean Engineering. World Scientific, Singapore.
Svendsen, I.A., Putrevu, U., 1993. Surf zone wave parameters from experimental data. Coastal Engineering 19, 283–310.
Symonds, G., Huntley, D.A., Bowen, A.J., 1982. Two dimensional surf beat: long wave generation by a time varying breakpoint. Journal of Geophysical Research 87 (C1), 492–498.
Thomson, J.S., Elgar, S., Raubenheimer, B., Herbers, T.H.C., Guza, R.T., 2006. Tidal modulation of infragravity waves via nonlinear energy losses in the surf zone. Geophysical Research Letters 33 (L05601). http://dx.doi.org/10.1029/2005GL025514.
Ting, F.C.K., Kirby, J.T., 1994. Observation of undertow and turbulence in a laboratory surf zone. Coastal Engineering 24, 51–80.
Torres-Freyermuth, A., Losada, I.J., Lara, J.L., 2007. Modeling of surf zone processes on a natural beach using Reynolds–Averaged Navier–Stokes equations. Journal of Geophysical Research 112 (L05601). http://dx.doi.org/10.1029/2006JC004050.
Torres-Freyermuth, A., Lara, J.L., Losada, I.J., 2010. Numerical modelling of short- and long-wave transformation on a barred beach. Coastal Engineering 57, 317–330.
Tucker, M.J., 1950. Surf beats: sea waves of 1 to 5 min. period. Proceedings of the Royal Society of London Series A 202, 565–573.
van Dongeren, A.R., 1997. Numerical modeling of quasi-3D nearshore hydrodynamics. Tech. rep. Cent. for Appl. Coastal Res., Univ. of Delaware, Newark.
van Dongeren, A.R., Battjes, J.A., Janssen, T.T., van Noorloos, J., Steenbergen, K., Reniers, A., 2007. Shoaling and shoreline dissipation of low-frequency waves. Journal of Geophysical Research 112 (C02011). http://dx.doi.org/10.1029/2006JC003701.